Bio-Design and Manufacturing (2026) 9:501–513
https://doi.org/10.1631/bdm.2500463

RESEARCH ARTICLE

Green staggered traveling-surface Rayleigh acoustic wave microchips for additive-free cell lysis

Haiwei Lu[1,2,6,7,8] · Rui Wang[2] · Lavonda Li[3,4] · Shichao Ding[3,5] · Lijie Yan[3,9] · Senlin Wang[7] · Chaohui Wang[6] · Tengfei Zheng[6] · Junying Sun[1] · Xingcai Zhang[2,3,4,5]

Received: 11 September 2025 / Accepted: 11 January 2026

Abstract

Efficient coupling between acoustic fields and fluid microenvironments is crucial for advancing applied physics and microfluidic engineering in advanced biomedical, environmental sustainability, and broader industrial applications. Harnessing such interactions for biological processing enables the precise, contactless, and tunable control of cell membrane disruption, facilitating reagent-free, contamination-minimized lysis. However, existing acoustic lysis devices are faced with challenges of limited efficiency and intricate structures. To overcome these limitations, we developed a staggered traveling-surface Rayleigh acoustic wave (STRAW) microchip for additive-free cell lysis. The device consists of a $LiNbO_3$ substrate patterned with two sets of interdigital transducers and a circular polydimethylsiloxane ring for confining cell suspension. We constructed a mathematical model for the STRAW-induced mechanical effects and optimized the alignment of interdigital transducers via theoretical modeling and finite-element analysis to maximize torque and acoustic streaming. The proposed STRAW-based platform showed over 95% lysis efficiency within 30 s for MC3T3-E1 mammalian cells, Gram-negative *Escherichia coli*, and Gram-positive *Staphylococcus aureus*. Thus, the developed design enables additive-free, structurally straightforward acoustic lysis with demonstrated compatibility across the tested cell types. Beyond basic lysis, this universal platform can be used in point-of-care diagnostics and food and environmental safety monitoring. This work illustrates how fluid structure–wave interactions may inform fluid mechanics and applied physics within a high-performance, low-complexity microfluidic system, paving the way for the widespread integration of STRAW-induced acoustic streaming in diagnostics, industry, and research.

✉ Tengfei Zheng
tengfz@xjtu.edu.cn

✉ Junying Sun
sunjy@hebtu.edu.cn

✉ Xingcai Zhang
xiz292@ucsd.edu

1 School of Engineering, Hebei Normal University, Shijiazhuang 050024, China

2 School of Engineering and Applied Sciences, Harvard University, Cambridge, MA 02138, USA

3 World Tea Organization, Cambridge, MA 02139, USA

4 Department of Materials Science and Engineering, Stanford University, Stanford, CA 94305, USA

5 Department of Chemical and Nano Engineering, University of California, San Diego, La Jolla, CA 92093, USA

6 State Key Laboratory for Manufacturing Systems Engineering, Xi'an Jiaotong University, Xi'an 710049, China

7 Fujian Provincial Key Laboratory of Intelligent Identification and Control of Complex Dynamic System, Quanzhou 362200, China

8 Hebei Provincial Key Laboratory of Information Fusion and Intelligent Control, Shijiazhuang 050024, China

9 Department of Medicine, Stanford University, Stanford, CA 94305, USA

Graphical abstract

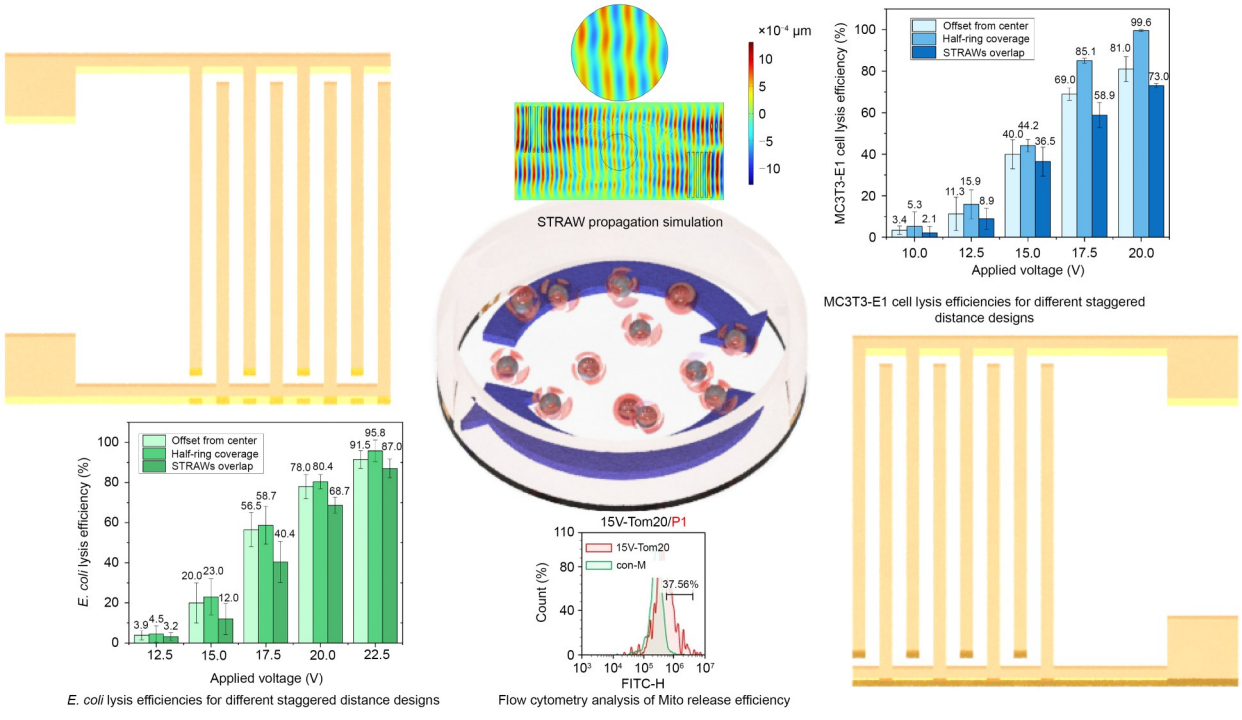

Keywords Staggered traveling-surface Rayleigh acoustic wave (STRAW) · Acoustic streaming · Microfluidics · Microchip for additive-free cell lysis (MAC) · Sustainability

1 Introduction

The rapid development of modern chemistry, molecular biology, gene therapy, and disease diagnosis has made investigations of intracellular contents, including DNA, RNA, and proteins that carry genetic information and disease-related signatures, increasingly critical for basic research and clinical applications [1–4]. Cell lysis, as an indispensable step for accessing these intracellular substances, has thus garnered increasing attention in recent years [5]. Commonly used lysis methods are categorized into chemical, biological, physical, or their combination [6, 7]. Chemical lysis relies on lysis buffers or surfactants to rupture cell membranes and release intracellular contents, whereas biological lysis employs various enzymes for cell breakdown. Although these two methods can achieve high extraction yields, they suffer from inherent limitations. Chemical lysis requires a series of operations, such as precise mixing, prolonged incubation, and complex sample pretreatment, accompanied by the use of large quantities of solvents that pose environmental risks [8]. Biological lysis is constrained by high specificity to cell types and potential interference with downstream analysis because of residual enzymes. In recent years, physical lysis, which uses external forces such as thermal energy, sound energy, and electrical energy to break cell membranes, has attracted increasing attention as a promising alternative to chemical and biological methods [9–11]. Unlike chemical and biological methods, physical lysis is cell type-independent and thus suitable for heterogeneous cell populations. However, existing physical lysis technologies still face key challenges that limit their application. Thermal lysis can denature temperature-sensitive biomolecules, such as proteins and enzymes, impacting their biological activity and structural integrity [12]. At the same time, traditional ultrasonic lysis, although solvent-free and efficient, relies on bulky equipment, and the uncontrollable high pressure and temperature generated during cavitation may damage the target analytes. Moreover, its poor compatibility with miniaturized systems restricts integration with small downstream analysis devices [13].

Microfluidics has shown substantial potential for miniaturization and high-throughput biological and clinical analyses, spanning sample pretreatment, chemical synthesis, and point-of-care testing [14–28]. Building on this, herein, we propose a green staggered traveling-surface Rayleigh acoustic wave (STRAW) microchip for additive-free cell lysis

(MAC). As a contactless active actuation strategy, STRAW employs surface acoustic waves, which have been applied in particle aggregation/separation, droplet manipulation, microfluidic mixing, and nanomaterial synthesis, owing to their concentrated energy, large driving force, and excellent integration compatibility [29–31]. When STRAW interacts with a liquid medium, it radiates acoustic energy into the liquid to generate pressure waves. The rapid attenuation of these pressure waves induces intense acoustic streaming, which in turn enhances fluid mixing and mass transfer [32–35]. A critical limitation of prior acoustic lysis approaches is that a single set of interdigital transducers (IDTs) often lacks the capacity to generate acoustic output with sufficient intensity or spatial distribution to achieve rapid and effective cell lysis. To address this shortcoming, existing methods typically employ supporting components, such as microparticles for collision enhancement, microfabricated surface structures for shear stress intensification, or chemical reagents for cell membrane weakening. However, these methods introduce additional steps, increase the complexity of device fabrication, and increase the risk of interfering with downstream analysis [36–38]. In contrast, the staggered IDT array in our STRAW MAC is designed to form rotational vortices to amplify the acoustic streaming velocity.

Herein, we demonstrate that STRAWs, driven by two sets of staggered IDTs, induce rotational vortices in the cell suspension, concentrating acoustic energy and thereby enabling efficient cell lysis through surface acoustic waves alone. This method eliminates the requirement for additives or complex microstructures. Thus, the proposed lysis approach is efficient, cost-effective, and environmentally friendly. Notably, we have validated its efficiency on prokaryotic bacterial cells, which are surrounded by rigid, multilayer cell envelopes, including peptidoglycan layers in Gram-positive bacteria, and are more resistant to mechanical disruption compared to eukaryotic cells. Without the use of any additives, our STRAW-based approach showed more than 95% lysis efficiency for bacteria within 30 s. Furthermore, we developed fluid mechanics models and mathematical functions to quantify the flow fields and acoustic energy distribution induced by STRAWs. These models and functions provide a theoretical basis for optimizing lysis conditions. Beyond bacterial lysis, STRAWs were employed for the lysis of diverse cell types, including MC3T3-E1 (mammalian cell), *Escherichia coli* (*E. coli*, Gram-negative bacterium), and *Staphylococcus aureus* (*S. aureus*, Gram-positive bacterium), indicating the versatility of the proposed approach. The STRAW-induced acoustic field and temperature distribution were monitored to infer the proposed lysis mechanism. Additionally, experiments involving DNA gel electrophoresis and the structural integrity assessment of proteins were conducted to evaluate the potential practical utility of lysis products.

2 Results and discussion

Herein, we designed a microchip containing two sets of IDTs patterned on the surface of a piezoelectric substrate to generate sufficient acoustic energy for cell lysis. When a modulated electrical signal is applied to the IDTs, staggered acoustic waves are generated and propagate along the free surface of the substrate. Upon encountering a circular polydimethylsiloxane (PDMS) ring positioned at the center between the two IDTs, where the cell suspension is held, the acoustic waves are converted to Rayleigh waves because of the difference in wave velocities between the substrate and the liquid, thereby inducing acoustic streaming within the liquid. This acoustic streaming generates shear forces in the liquid, and when combined with pressure waves that act on the cells, the combined mechanical action alters the membrane stress, induces cell deformation, and eventually causes cell rupture and release of their intracellular contents. The schematic of the chip is shown in Fig. 1a.

The IDTs are composed of a 20-nm Cr adhesive layer and an 80-nm Au layer deposited on the surface of a 128° *Y*–*X* lithium niobate ($LiNbO_3$) substrate via photolithography and lift-off. The designed IDTs have a center frequency of approximately 20 MHz, 20 finger pairs, and an aperture of 5 mm. The two IDTs are spaced 14 mm apart horizontally. The PDMS ring is placed at the center between the two sets of IDTs and bound to the substrate through oxygen-plasma treatment, confining the cell suspension. The inner radius of

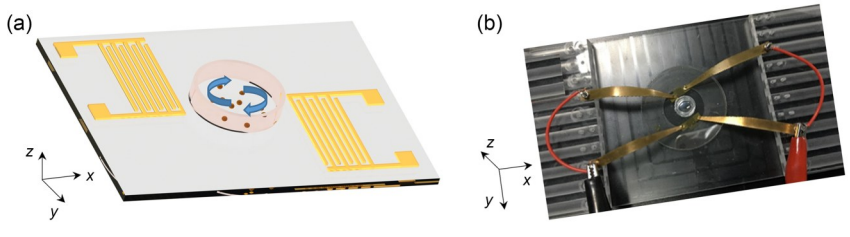

Fig. 1 Schematic illustration and fabricated device of the staggered traveling-surface Rayleigh acoustic wave (STRAW) microchip for additive-free cell lysis (MAC). (a) Schematic of the STRAW microchip, in which two groups of traveling surface acoustic waves propagate in opposite directions toward a circular PDMS ring loaded with cell suspension. (b) The fabricated MAC consists of two sets of IDTs deposited on the surface of the $LiNbO_3$ substrate with a PDMS ring

the PDMS ring is 4.5 mm. Both sets of IDTs are simultaneously excited using an alternating current (AC) signal generator (AFG3251C, Tektronix, USA), with the electrical signals amplified by a power amplifier (BA4850, NF, Japan). The fabricated cell lysis device is shown in Fig. 1b.

As the two sets of IDTs are staggered on two sides of the PDMS ring, the two sets of STRAWs propagate in opposite directions toward the liquid–solid interface. Because of the mismatch in acoustic velocity between solids and liquids, part of the waves propagates onward as a Rayleigh wave on the substrate, whereas the remainder refracts into the fluid as longitudinal waves at the Rayleigh angle. This wave–fluid interaction generates a body force that drives internal fluid motion within the liquid, a phenomenon called acoustic streaming.

Assuming that the fluid is incompressible and ignoring heat exchange with the external environment, the acoustic streaming within the droplet can be described using the Navier–Stokes equation and the continuity equation [32, 39]:

$$\nabla \cdot \boldsymbol{U} = 0, \tag{1}$$

$$\frac{\partial \boldsymbol{U}}{\partial t} + (\boldsymbol{U} \cdot \nabla)\boldsymbol{U} = -\frac{1}{\rho}\nabla p + \upsilon \nabla^2 \boldsymbol{U} + \boldsymbol{f}_{\mathrm{B}}, \tag{2}$$

where $\boldsymbol{U}$ is the acoustic streaming velocity (m/s), $\boldsymbol{f}_{\mathrm{B}}$ is the STRAW-induced nonlinear body force per unit volume (N/m^3), ρ is the fluid density (kg/m^3), p is the pressure (Pa), and υ is kinematic viscosity (m^2/s). When the acoustic wave propagates in the fluid, its vibration velocity drives fluid movement via Reynolds stress, and the spatial gradient of the Reynolds stress induces a body force. The vibration velocity can be obtained using the time derivative of the vibration displacement field of the acoustic wave. Reynolds stress originates from this vibration velocity field, and its spatial divergence generates a nonlinear body force in the planar domain (F_{B}), given by

$$F_{\mathrm{B}} = -\rho\left(1+\alpha^2\right)A^2\omega^2 k_i \exp\left(2\left(k_i x + \alpha k_i y\right)\right), \tag{3}$$

where α is the attenuation coefficient, A is the STRAW amplitude at the liquid entry point (m), $\omega = 2\pi f$ is the angular frequency (rad/s), k_i is the STRAW wavenumber, and x and y denote the horizontal and vertical coordinates, respectively. We investigated the body force by varying the staggered distance between IDTs, with the effects of other parameters not considered. The body force is proportional to the square of the amplitude (A^2) on the piezoelectric substrate. Symmetrically distributed STRAWs produce two parallel body forces that induce a torque within the fluid (Fig. 2a). Assuming that energy loss owing to acoustic radiation into the PDMS ring is negligible, the body force exerted on the fluid by the STRAWs can be considered uniformly distributed. The magnitude of the torque generated by this body force is

$$T = KA^2 l, \tag{4}$$

where T is the torque, l is the distance from the geometric center of the ring to the equivalent action point of the uniform body force, and K is

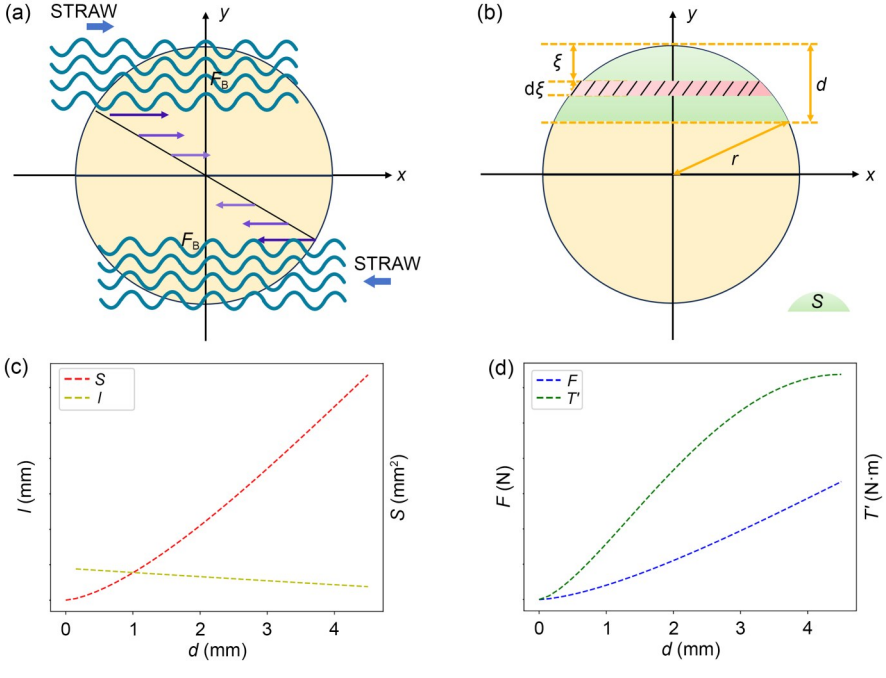

Fig. 2 Theoretical analysis of the STRAW staggered distance. (a) Schematic of body forces and the resulting torque induced by STRAWs. (b) Schematic illustrating key physical quantities. (c) Variations in the distance between the force action point and ring center (l) and STRAW coverage area (S) with respect to the STRAW coverage width on one side of the ring (d). (d) Relationships between torque (T'), acoustic streaming force (F), and STRAW coverage width on one side of the ring (d)

$$K = F_B / A^2 = -\rho\left(1+\alpha^2\right)\omega^2 k_i \exp\left(2\left(k_i x + \alpha k_i y\right)\right). \quad (5)$$

The magnitude of fluid torque is positively correlated with the acoustic streaming velocity, and its value depends on A and l. Herein, we adopted the integral method to calculate the total torque magnitude generated within the fluid region. The integration of the torque across the fluid domain yields

$$T' = K \iint A^2 l \mathrm{d}x\mathrm{d}y. \quad (6)$$

Let d denote the coverage width of STRAWs on one side of the PDMS ring. Assuming no attenuation and a uniform body force acting on each infinitesimal element within the STRAW-covered area, integration yields the relationships described in Eqs. (7) and (8) between distance l and parameter d and between the coverage area S and d, respectively. The total torque magnitude (T') and the magnitude of the total equivalent force (F) are given in Eq. (9).

$$l = \frac{T'}{F} = \frac{\int_0^d \sqrt{r^2 - (r-\xi)^2}\,(r-\xi)\,\mathrm{d}\xi}{\int_0^d \sqrt{r^2 - (r-\xi)^2}\,\mathrm{d}\xi}, \quad (7)$$

$$S = 2\int_0^d \sqrt{r^2 - (r-\xi)^2}\,\mathrm{d}\xi, \quad (8)$$

$$T' = F \times l, \quad (9)$$

$$T' = 2F_B \int_0^d (r-\xi)\sqrt{r^2 - (r-\xi)^2}\,\mathrm{d}\xi, \quad (10)$$

where the definitions of key parameters (coverage width d and coverage area S) and relationships between them are directly labeled in Fig. 2b for clarity. The variations in the distance from the uniform force action point to the ring center (l), the STRAW coverage area on one side (S), total torque (T'), and acoustic streaming force (F) with respect to d are shown in Figs. 2c and 2d. The results indicate that STRAWs move closer to the ring center with increasing d, expanding the coverage area and enhancing the streaming force and torque. The torque reaches the maximum value, and the peak of the acoustic streaming effect occurs when STRAWs cover half of the ring area.

To quantify how the IDT staggered distance impacts the amplitude of substrate vibration, we investigated the propagation characteristics of STRAWs using finite-element simulations, where STRAWs were excited and propagated along a linear direction. Figures 3a1, 3b1, and 3c1 show the relative positions of the IDTs and the PDMS ring at different staggered distances: Fig. 3a1 shows the offset of the IDTs from the PDMS ring center, Fig. 3b1 exhibits the configuration where two sets of STRAWs cover half of the ring area, and Fig. 3c1 presents the configuration where the two sets of STRAWs overlap within the PDMS ring. Figures 3a2, 3b2, and 3c2 show the amplitude distributions under the same input voltage for the above three configurations, respectively. The circular area denotes the fluid domain, with a zoomed-in view of this region providing a clearer visualization of the vibrational characteristics. For quantitative analysis, three cross-sectional lines were set along the central axis of the ring and above/below the central axis (positions shown in Figs. 3a1, 3b1, and 3c1, with the corresponding vibrational displacement presented in Figs. 3a3, 3b3, and 3c3). Figures 3a3 and 3b3 show that the substrate amplitude is considerably higher when the STRAWs excited by the IDTs are closer to the ring center (Fig. 3b1 configuration). When STRAWs overlap (Fig. 3c1 configuration), the amplitudes along all three cross-sections (Fig. 3c3) are higher than those at the corresponding positions in Figs. 3a1 and 3b1 configurations (Figs. 3a3 and 3b3). However, the intersection of the two sets of STRAWs leads to the formation of standing waves with a periodic acoustic pressure distribution, causing the energy to oscillate at fixed locations without net energy transfer [40]. Traveling waves are more conducive to generating strong acoustic streaming, whereas standing waves inhibit the formation of large vortices in the fluid region, which is detrimental to cell lysis [41–43]. Consequently, the substrate amplitude is the highest when the STRAWs exactly cover half of the ring (Fig. 3b1 configuration). In this configuration, the two sets of STRAWs generate a pair of symmetric, counterdirectional forces within the microfluidic region. The resulting torque drives fluid motion, inducing the deformation of the liquid–air interface and generating strong acoustic streaming vortices. Because each group of STRAWs covers about half of the ring, the cell suspension within the circular ring rotates around its vertical axis because of the increased angular momentum. The streaming velocity and shear rate inside the spinning droplet can be 10–100 times higher than those in the nonspinning droplet [44]. Cells in the suspension are affected by the vortex-shaped streamline and by the angular momentum of the continuously rotating vortex field. This combined effect alters the membrane stress, induces cell deformation, and ultimately promotes cell lysis. Notably, several simplifying assumptions usually used in two-dimensional (2D) mechanistic modeling (uniform body force, negligible attenuation, and omission of PDMS energy dissipation) were employed in the above derivation [45, 46]. In our symmetric device design, these assumptions were consistently applied to the upper and lower symmetric regions of the PDMS ring. Given the structural symmetry, the biases introduced by these simplifications are identical across symmetric regions and thus mutually cancel out.

We further investigated the role of input voltage under the optimal staggered configuration (half-ring coverage). When the two sets of IDTs cover exactly half of the ring (Fig. 3b1 configuration), the amplitude distribution increases with input voltage (10, 14, and 18 V), as shown in Figs. 4a–4c.

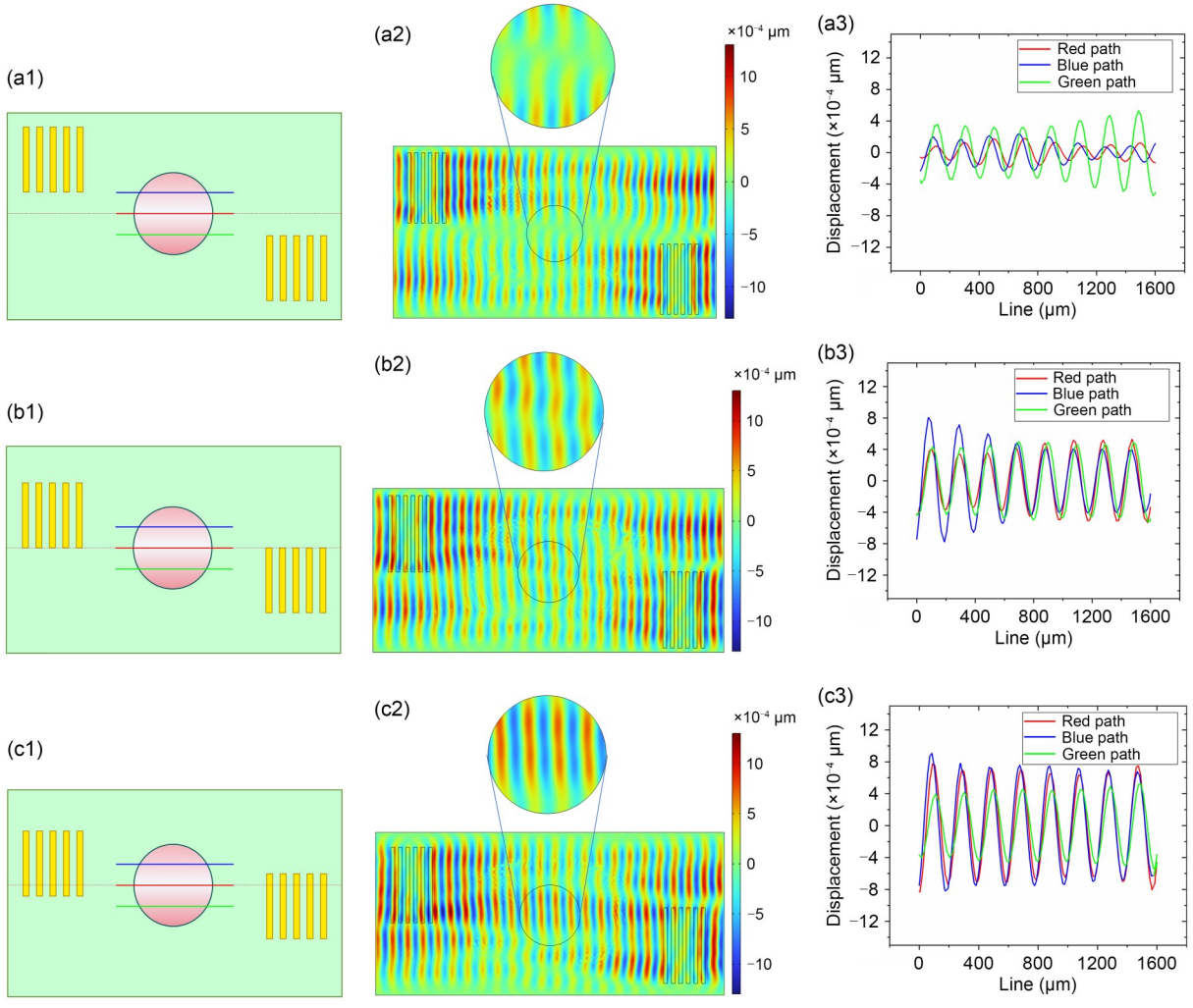

Fig. 3 Effect of IDT staggered distance on the propagation characteristics of STRAWs. (a1, b1, c1) Schematics of the relative positions of IDTs and the PDMS ring: (a1) offset from center; (b1) half-ring coverage; (c1) STRAWs overlap. (a2, b2, c2) Amplitude distributions under corresponding configurations (input voltage of 15 V). (a3, b3, c3) Vibrational displacement along cross-sections at the central axis (red), above the central axis (blue), and below the central axis (green), i.e., positions indicated by solid lines of corresponding colors in (a1), (b1), and (c1)

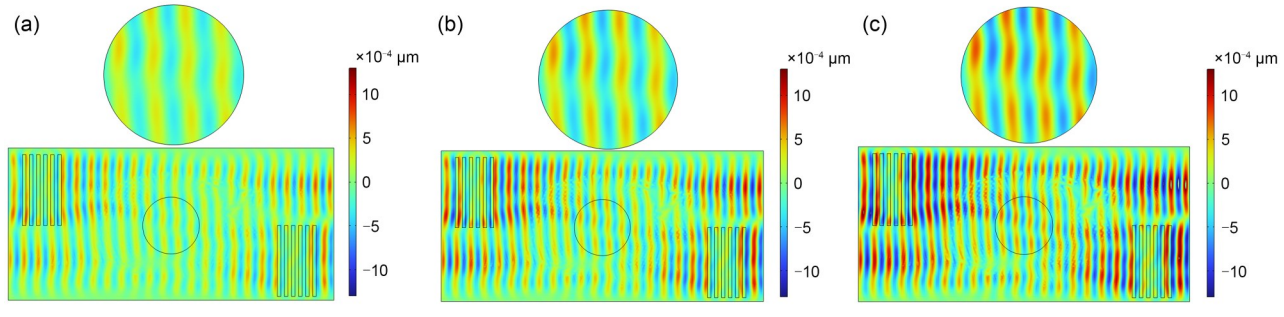

Fig. 4 Effect of input voltage on amplitude in the half-ring coverage configuration. (a–c) STRAW propagation simulations at input voltages of 10 V (a), 14 V (b), and 18 V (c) in the half-ring coverage configuration. The circular area represents the fluid domain

The zoomed-in views of the fluid domain clearly show that the peak amplitude increases with voltage. This result also validates the theoretical prediction derived from the body force equation, providing a foundational basis for regulating the intensity of acoustic streaming via voltage control.

To evaluate the lysis performance of the designed chip, we conducted a series of experiments. We used MC3T3-E1 (mouse embryo osteoblast precursor cells), *E. coli* (Gram-negative bacteria), and *S. aureus* (Gram-positive bacteria) as lysing objects. For experimental consistency, the concentration

of MC3T3-E1 cells was adjusted to 2×10^5 cells/mL, whereas the concentrations of *E. coli* and *S. aureus* were set to 2×10^9 cells/mL. These concentrations were held constant throughout all experiments. We added 50 μL of the cell suspension to the PDMS ring using a pipette. The input voltage of the signal generator was tuned within a range of 2.0–4.5 V. Therefore, the voltage applied to the IDT bus-bar was 10.0–22.5 V after a five-time amplification by the signal amplifier. As the input voltage increased, cells were driven by high-speed acoustic streaming and lysed via the combined action of shear forces and acoustic pressure. We tested the lysis durations of 5–30 s and, immediately after lysis, removed the lysate suspension from the PDMS ring using a pipette for subsequent analysis. To prevent cross-contamination between trials, we washed the PDMS ring area with deionized water before and after each experiment.

To distinguish and visualize the live and dead cells, as well as directly verify whether STRAWs induce membrane damage, we stained MC3T3-E1 cells with Trypan Blue before and after exposure to the acoustic field and observed them via microscopy. This stain dyes cells with impaired membranes blue but cannot penetrate the membrane of living cells with intact membranes. Before the STRAW treatment, almost all cells remained in their original stereoscopically transparent state. In contrast, with increasing input voltage, a growing proportion of cells were stained blue, indicating an increasing proportion of cells with damaged membranes (Figs. 5a–5d).

As higher input voltage enhances the shear rate and acoustic pressure exerted on the cell suspension, we further investigated the relationship between input voltage and lysis efficiency at a fixed lysis duration. For bacteria samples, we collected the cell suspension after exposure to the acoustic field, and then diluted and plated them on a Luria-Bertani (LB) agar plate. We counted the colonies and calculated the number of cell samples after 12 h of incubation. For MC3T3-E1 cells, we used Trypan Blue to determine the number of live and dead cells. In each experiment, we used a cell suspension kept on ice as a control group to accurately determine the number of viable cells before exposure to the acoustic field.

When an electrical signal with an input voltage below 10.0 V is applied to the two sets of IDTs, the suspension in the PDMS ring exhibits only minor oscillations, with the cells in the suspension barely affected because of insufficient acoustic radiation pressure and acoustic streaming intensity. With increasing input voltage, vortex streaming is enhanced, leading to slight oscillations on the suspension surface and the exposure of cells in the suspension to acoustic pressure and streaming effects. With a continued increase in the input voltage, the acoustic streaming strengthens, and the suspension begins to rotate within the PDMS ring. As a result, cells in the suspension experience strong shear forces. For *E. coli*, the lysis efficiency reaches approximately 95.8% at an input voltage of 22.5 V (Fig. 6a). At the same time, for MC3T3-E1 cells, a lysis efficiency of about 99.6% is achieved at an input voltage of 20 V (Fig. 6b). To validate

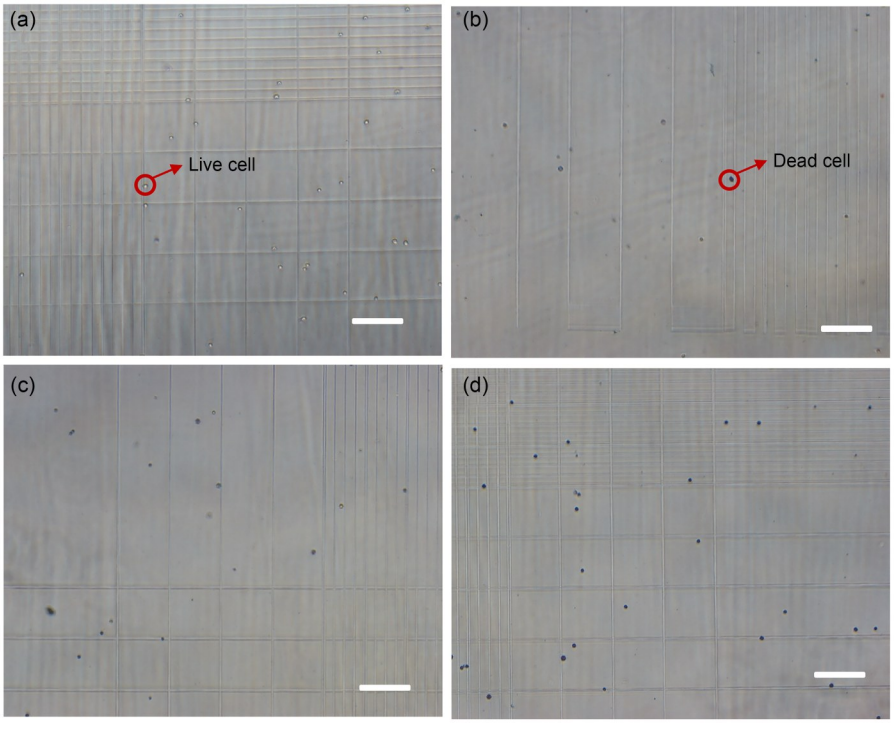

Fig. 5 Images of MC3T3-E1 cells stained with Trypan Blue. (a) Untreated control. (b–d) Cells after 30 s of exposure to STRAWs at an input voltage of 15.0 V (b), 17.5 V (c), and 20.0 V (d). Scale bars: 250 μm

the effectiveness of the optimized half-ring coverage layout, we additionally designed chips with two alternative staggered distances: one with a 3-mm offset between the two IDT groups (corresponding to the configuration in Fig. 3a1) and the other with a 2-mm overlap between the two IDT groups (Fig. 3c1 configuration). Lysis efficiencies for all three designs are presented in Fig. 6. The half-ring coverage configuration yields the highest lysis efficiency, followed by the 3-mm offset design, whereas the 2-mm overlap exhibits the lowest lysis efficiency among the three. These results were attributed to the formation of approximately 2-mm-wide standing surface acoustic waves (SAWs) within the ring, hindering the generation of high-speed acoustic streaming. These results are consistent with our theoretical derivation and simulation outcomes. To ensure data reliability, each data point was tested three times on the same chip, and all experimental conditions were replicated on three different chips on separate dates.

We also investigated how lysis efficiency varies with lysis duration. For *E. coli* at an input voltage of 22.5 V, fewer than 15% of cells were lysed at a lysis duration below 10 s, whereas 42.2% of cells were lysed at 15 s and 95.8% at 30 s (Fig. 7a). For MC3T3-E1 cells at 20.0-V input voltage, the lysis efficiency reaches 48.0% at 10 s and 97.9% at 25 s (Fig. 7b). To assess the lysing capability of the device across different microbial strains, we tested it on *S. aureus*, Gram-positive bacteria. When 50 μL of *S. aureus* suspension with a concentration of 2×10^9 cells/mL was added to the PDMS ring, the device achieved 96.6% lysis efficiency at 22.5 V input voltage and 30 s lysis duration.

Local heating is a common concern in SAW-driven systems. To address this potential issue, we tracked real-time temperature changes under all operating conditions by conducting temperature-monitoring experiments using an infrared thermal imaging system (Fig. 8a). The maximum temperature within the PDMS ring for each applied voltage is plotted in Fig. 8b. The results indicate a time-dependent temperature increase at all voltages. At lower voltages (10.0 and 12.5 V), the maximum temperature within the PDMS ring does not exceed 40 °C throughout the 30-s period. At higher voltages (20.0 and 22.5 V), the maximum temperature is substantially higher, reaching nearly 70 °C at the 30-s mark.

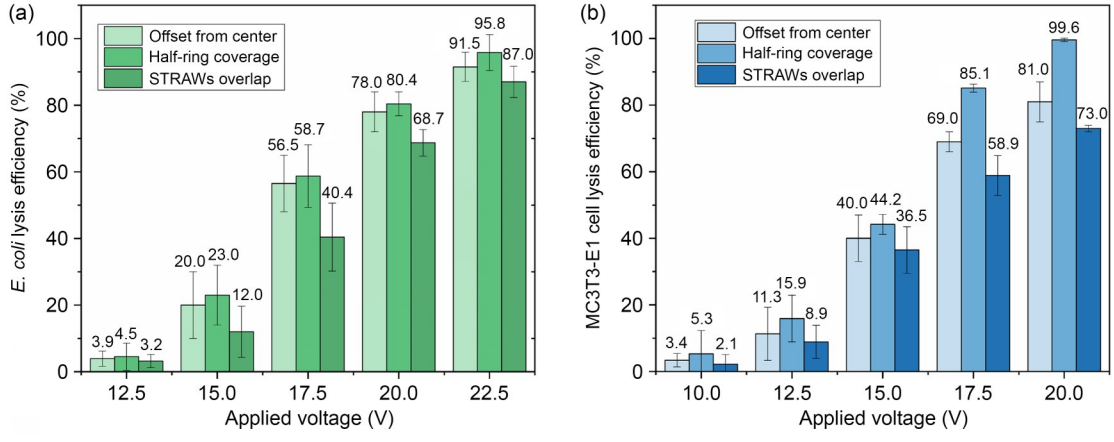

Fig. 6 Lysis efficiency at different input voltages and a lysis duration of 30 s for different staggered distance designs: (a) *E. coli*; (b) MC3T3-E1 cells

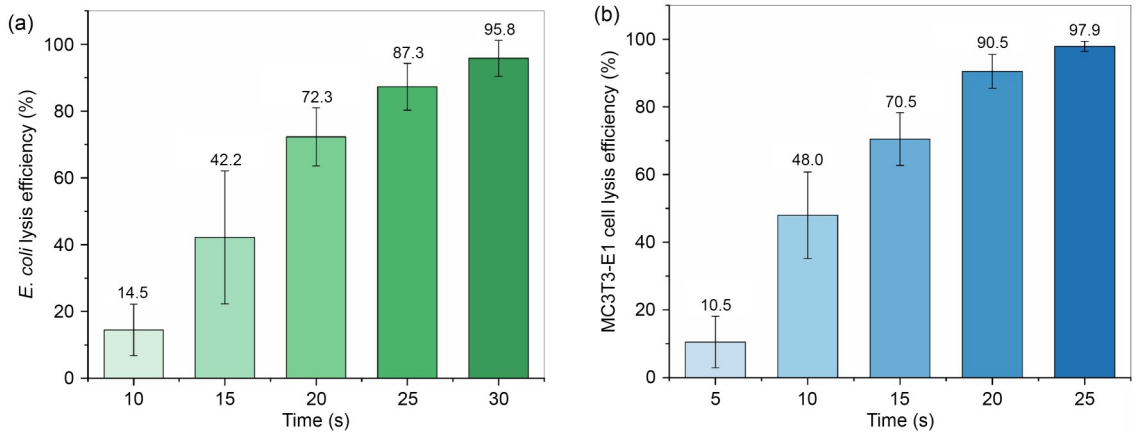

Fig. 7 Lysis efficiency at different lysis times for *E. coli* under 22.5 V input voltage (a) and for MC3T3-E1 cells under 20.0 V input voltage (b)

However, it is important to note that the reported values reflect peak temperatures captured via infrared imaging, whereas the average temperature across the entire PDMS ring region is lower. Additionally, the temperature increase starts from an ambient temperature baseline of about 17 °C, implying that the actual average temperature experienced by cells during lysis is lower than the recorded peak values. According to the literature, a purely thermal lysis of *E. coli* requires exposure to temperatures exceeding 60 °C for approximately 15 s [47]. In our system, the maximum temperature exceeds 60 °C after 25 s at the highest applied voltage (22.5 V), and under all other operating conditions, the temperature is below this value, indicating that the lysis is thermally assisted. To verify the STRAW-induced fluid pattern, we designed a two-phase mixing experiment using rhodamine-labeled aqueous solution and glycerol, recording the fluid motion dynamics during acoustic wave actuation (Video S1 in the supplementary information). As shown in Fig. 8c, when rhodamine solution was injected into glycerol and a 20.0-V SAW was applied, the rhodamine solution exhibited distinct circular movement, consistent with the expected pattern of STRAW-driven acoustic streaming.

To evaluate the protein release efficiency and the retention of biomolecular functionality, we treated AML12 cells using our STRAW device and analyzed the resulting lysates via flow cytometry (FC; Fig. 9a). The results indicate that the STRAW treatment substantially enhanced the release of proteins from subcellular compartments, including the endoplasmic reticulum and mitochondria, compared with the control group. As our FC experiments employed the antigen–antibody binding assay, which inherently relies on the structural integrity of target proteins, the FC results also provide direct evidence that these released proteins retained their structural stability. To further verify the lysis products, we performed electrophoresis on the *E. coli* lysate. We centrifuged the *E. coli* sample taken from the PDMS ring to obtain the supernatant, which excluded intact cells and cell debris. We loaded the supernatant on a 1% agarose gel, ran it under 100 V for 35 min, and imaged it under an ultraviolet lamp. The electrophoresis results are shown in Fig. 9b. The left

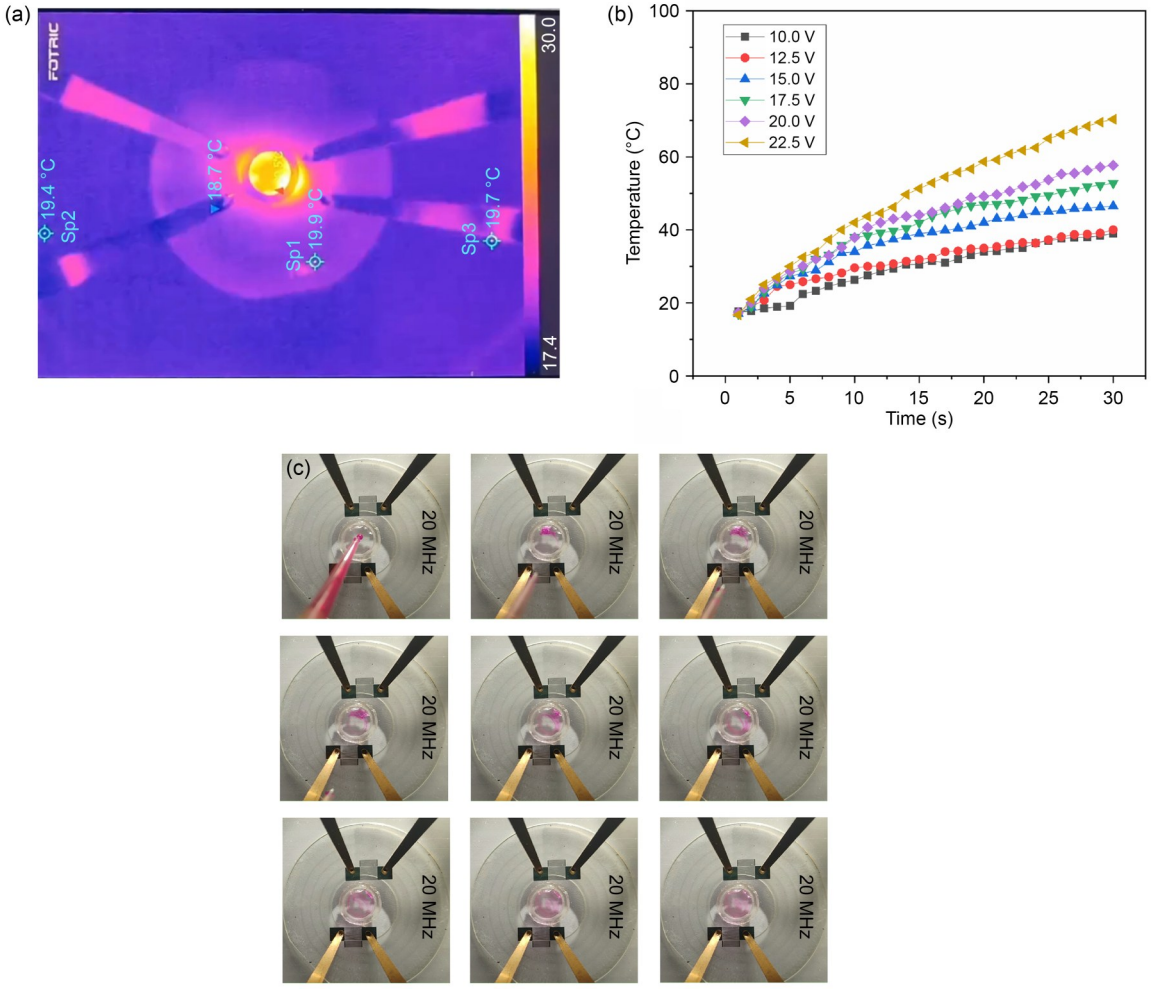

Fig. 8 Device characterization results. (a) Temperature distribution at 14 s under 10.0 V. (b) Maximum temperature versus time under different applied voltages. (c) Image sequence of the STRAW-driven fluid experiment

column is the DNA band. "STRAW lysate" in the second column represents the cell lysate obtained at 22.5 V input voltage and 30 s lysis time. The "control group 1" and "control group 2" denote 1/2 of the lysates and all lysates from an equivalent number of *E. coli* cells using the Takara genomic DNA extraction kit. The results indicate the presence of nucleic acids in the supernatant, consistent with high-molecular-weight genomic DNA.

Additionally, compared with existing SAW lysis techniques, our method does not require the use of additives and is compatible with a broader range of cell types, as summarized in Table 1. Notably, direct benchmarking against conventional methods (sonication or chemical lysis) was not performed because of inherent differences in their intended application scenarios and operational requirements, including sample volume, processing workflow, and integration potential.

3 Device fabrication

We fabricated IDTs on the piezoelectric substrate via ultraviolet lithography and lift-off, following a standardized microfabrication workflow. A 128° *Y*–*X* $LiNbO_3$ wafer was selected as the piezoelectric substrate. The wafer had a diameter of 2 inches (1 inch=0.0254 m) and a thickness of approximately 1 mm, with both surfaces polished. The IDT patterns were designed in AutoCAD and transferred to a photomask for lithography. After sequential cleaning with acetone, ethanol, and deionized water, the $LiNbO_3$ wafer was spin-coated with EGP533 photoresist (Electronic Chemicals, Thailand; 500 r/min for the initial spin, followed by 1000 r/min for 40 s) and soft-baked at 95 °C for 5 min. Next, pattern alignment and ultraviolet exposure were conducted using a mask aligner (ABM, USA). A postexposure bake (95 °C, 5 min) was performed, after which the wafer was developed in 0.5% NaOH solution for approximately 65 s. Subsequently, a 20-nm Cr adhesive layer and an 80-nm Au layer were sequentially deposited on the wafer via electron-beam evaporation (TF500, HHV, UK). Finally, the IDTs were formed through lift-off in acetone under ultrasonication for approximately 3 h. For the fabrication of the PDMS ring, a 3D-printed mold was used to define the ring geometry. The PDMS prepolymer (Sylgard 184, SYLGARD, USA; 10:1 (base:curing agent))

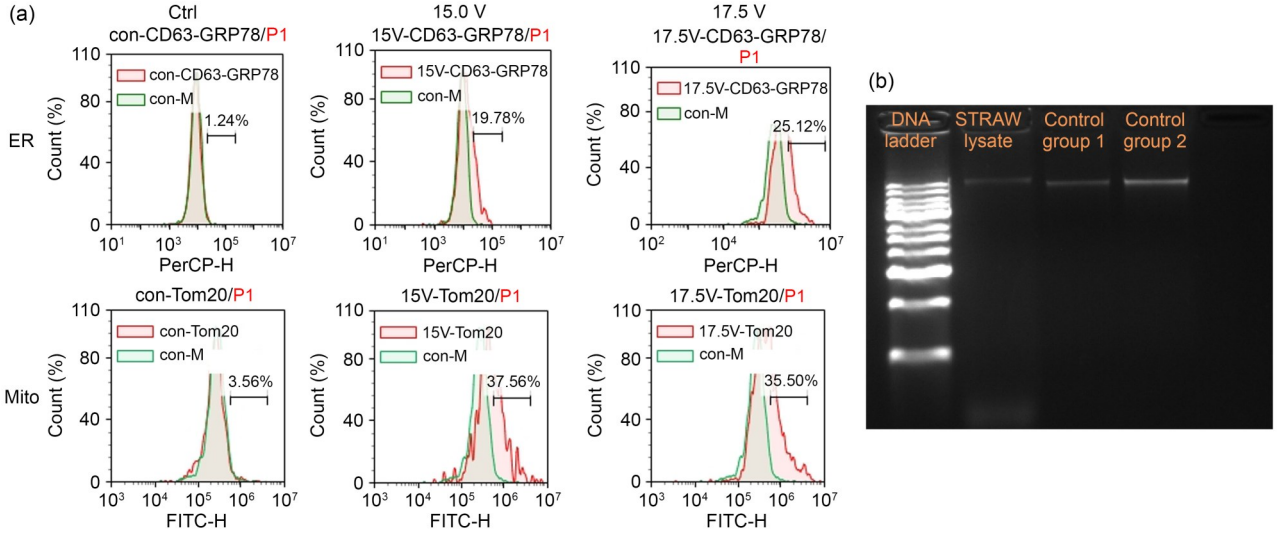

Fig. 9 Verification of genetic content release from lysates. (a) FC analysis of protein release efficiency. (b) Electrophoresis results for the *E. coli* lysate. ER: endoplasmic reticulum

Table 1 Comparison of SAW-based cell lysis technologies

Device	Requirement of additives/microbeads	Cell type	Lysis time	Lysis efficiency	Sample volume	Ref.
IDT, SU8 micropillars, and fluid chamber	Micropillar	Mouse embryonic fibroblasts	20 s	95%	10–30 μL cell solution droplets	[38]
IDT and phononic lattice	Sample in oil	*P. berghei*-infected RBCs and *T. cyclops*	<10 s	>98%	5–20 μL blood cells/parasite droplet	[36]
IDT and 3M tape	4-μm magnetic microparticles	MDA-MB-231, MCF-7, and hADSC	20 s	92%–100%	5–10 μL droplets	[37]
IDT and PDMS ring	No additives/ microstructures	MC3T3-E1, *E. coli*, and *S. aureus*	25–30 s	95.8%–99.6%	50 μL cell suspension	This work

P. berghei: *Plasmodium berghei*; RBC: red blood cell; *T. cyclops*: *Trypanosoma cyclops*; hADSC: human adipose-derived stem cell

was mixed, degassed to eliminate air bubbles, poured onto the 3D-printed mold, and cured at 65 °C. The cured PDMS ring was then peeled from the mold. To achieve bonding, the PDMS ring and $LiNbO_3$ substrate surfaces were treated with activated oxygen plasma (30 W, 10 s). The PDMS ring was aligned on the substrate and bound to it under a microscope. Finally, permanent bonding was achieved by heating the assembly on a 150 °C hotplate for 5–10 min.

4 Conclusions

Herein, we developed an additive-free microfluidic device that employs STRAWs to lyse a small amount of cell suspension. Two sets of IDTs were patterned in a staggered configuration on a $LiNbO_3$ substrate to direct counterpropagating STRAWs toward the PDMS ring at the center between the IDTs, driving the rotational motion of the enclosed cell suspension. Through a combination of theoretical modeling, finite-element analysis, and experiments, we identified the half-ring coverage IDT layout as the optimal structural configuration. In this configuration, cells in the spinning suspension are subjected to shear forces and acoustic pressure. Infrared thermal imaging confirmed that thermal effects from SAW excitation provide an auxiliary role that does not compromise the biomolecular mechanism. Therefore, mechanical forces are proposed as the dominant lysis mechanism, with thermal effects assisting in disrupting cellular membranes and facilitating the release of intracellular components. We further established that lysis efficiency is positively correlated with input voltage and treatment duration. We achieved above 95% lysis efficiency for Gram-negative (*E. coli*) and Gram-positive (*S. aureus*) bacteria within 30 s and a 99.6% lysis efficiency for MC3T3-E1 mouse embryo osteoblast precursor cells within 30 s, indicating the suitability of the proposed method for rapid, reagent-free, cell type-independent lysis applications. We verified the cell contents via gel electrophoresis and FC, which indicated the successful release of structurally intact nucleic acids and subcellular proteins. Compared with conventional SAW lysis techniques, our device eliminates the need for chemical additives or complex channel geometries and achieves high lysis efficiency across diverse cell types (mammalian cells and bacteria). Future work may focus on scaling the device for high-throughput applications, integrating it with on-chip sample preprocessing modules, evaluating the specific functional attributes of the released biomolecules, and expanding its compatibility with specialized cellular samples to advance point-of-care diagnostic platforms as well as food and environmental safety monitoring.

Supplementary Information The online version contains supplementary material available at https://doi.org/10.1631/bdm.2500463.

Acknowledgements This work was supported by the Science Foundation of Hebei Normal University (No. L2023B43), the Open Project Program of Fujian Provincial Key Laboratory of Intelligent Identification and Control of Complex Dynamic System (No. 2023A0005), and the Central Guided Local Science and Technology Development Fund Project (No. 246Z0302G).

Declarations

Conflict of interest The authors declare that they have no conflict of interest.

Ethical approval This study did not involve human or animal subjects. MC3T3-E1 cells were obtained from the Cell Bank of the Chinese Academy of Sciences (Shanghai, China). AML12 cells were obtained from the American Type Culture Collection (ATCC, Manassas, VA, USA; CRL-2254). No additional ethical approval was required for the use of these commercial cell lines.

Data availability The data that support the findings of this study are available from the corresponding authors upon reasonable request.

Use of generative AI tools During the preparation of this work, the authors used DeepSeek to improve language and readability. After using this tool, the authors reviewed and edited the contents as needed and take full responsibility for the content of the publication.

References

1. Das S, Vera M, Gandin V et al (2021) Intracellular mRNA transport and localized translation. *Nat Rev Mol Cell Biol* 22(7): 483–504. https://doi.org/10.1038/s41580-021-00356-8
2. Li X, Zhang WJ, Li HL et al (2025) Sprayed aqueous microdroplets for spontaneous synthesis of functional microgels. *Angew Chem Int Ed* 64(8):e202420926. https://doi.org/10.1002/anie.202420926
3. Qian J, Xia JP, Chiang S et al (2025) Rapid and comprehensive detection of viral antibodies and nucleic acids via an acoustofluidic integrated molecular diagnostics chip: AIMDx. *Sci Adv* 11(3): eadt5464. https://doi.org/10.1126/sciadv.adt5464
4. Rohner E, Yang R, Foo KS et al (2022) Unlocking the promise of mRNA therapeutics. *Nat Biotechnol* 40(11):1586–1600. https://doi.org/10.1038/s41587-022-01491-z
5. Paul R, Ostermann E, Wei QS (2020) Advances in point-of-care nucleic acid extraction technologies for rapid diagnosis of human and plant diseases. *Biosens Bioelectron* 169:112592. https://doi.org/10.1016/j.bios.2020.112592
6. Neuwirt E, Magnani G, Ćiković T et al (2023) Tyrosine kinase inhibitors can activate the NLRP3 inflammasome in myeloid cells through lysosomal damage and cell lysis. *Sci Signal* 16(768): eabh1083. https://doi.org/10.1126/scisignal.abh1083
7. Nair G, Jain V (2024) An intramolecular cross-talk in D29 mycobacteriophage endolysin governs the lytic cycle and phage-host population dynamics. *Sci Adv* 10(6):eadh9812. https://doi.org/10.1126/sciadv.adh9812
8. Britt HM, Prakash AS, Appleby S et al (2020) Lysis of membrane lipids promoted by small organic molecules: reactivity depends on structure but not lipophilicity. *Sci Adv* 6(17):eaaz8598. https://doi.org/10.1126/sciadv.aaz8598

9. Wen CT, Zhang JX, Zhang HH et al (2018) Advances in ultrasound assisted extraction of bioactive compounds from cash crops – a review. *Ultrason Sonochem* 48:538–549. https://doi.org/10.1016/j.ultsonch.2018.07.018
10. Nan L, Jiang ZD, Wei XY (2014) Emerging microfluidic devices for cell lysis: a review. *Lab Chip* 14(6):1060–1073. https://doi.org/10.1039/c3lc51133b
11. Wu Y, Fu AF, Yossifon G (2020) Active particles as mobile microelectrodes for selective bacteria electroporation and transport. *Sci Adv* 6(5):eaay4412. https://doi.org/10.1126/sciadv.aay4412
12. Leuenberger P, Ganscha S, Kahraman A et al (2017) Cell-wide analysis of protein thermal unfolding reveals determinants of thermostability. *Science* 355(6327):eaai7825. https://doi.org/10.1126/science.aai7825
13. Shen LP, Pang SX, Zhong MM et al (2023) A comprehensive review of ultrasonic assisted extraction (UAE) for bioactive components: principles, advantages, equipment, and combined technologies. *Ultrason Sonochem* 101:106646. https://doi.org/10.1016/j.ultsonch.2023.106646
14. Chowdhury MS, Zheng WS, Kumari S et al (2019) Dendronized fluorosurfactant for highly stable water-in-fluorinated oil emulsions with minimal inter-droplet transfer of small molecules. *Nat Commun* 10:4546. https://doi.org/10.1038/s41467-019-12462-5
15. Mo YM, Lu ZH, Rughoobur G et al (2020) Microfluidic electrochemistry for single-electron transfer redox-neutral reactions. *Science* 368(6497):1352–1357. https://doi.org/10.1126/science.aba3823
16. Tang ZM, Kong N, Zhang XC et al (2020) A materials-science perspective on tackling COVID-19. *Nat Rev Mater* 5(11):847–860. https://doi.org/10.1038/s41578-020-00247-y
17. Wang YH, Lu L, Zheng GX et al (2020) Microenvironment-controlled micropatterned microfluidic model (MMMM) for biomimetic *in situ* studies. *ACS Nano* 14(8):9861–9872. https://doi.org/10.1021/acsnano.0c02701
18. Chowdhury MS, Zhang XC, Amini L et al (2021) Functional surfactants for molecular fishing, capsule creation, and single-cell gene expression. *Nano-Micro Lett* 13(1):147. https://doi.org/10.1007/s40820-021-00663-x
19. Kim C, Hong S, Shin D et al (2021) Sorting gold and sand (silica) using atomic force microscope-based dielectrophoresis. *Nanomicro Lett* 14(1):13. https://doi.org/10.1007/s40820-021-00760-x
20. Liu LB, Bi MC, Wang YH et al (2021) Artificial intelligence-powered microfluidics for nanomedicine and materials synthesis. *Nanoscale* 13(46):19352–19366. https://doi.org/10.1039/d1nr06195j
21. Markin CJ, Mokhtari DA, Sunden F et al (2021) Revealing enzyme functional architecture via high-throughput microfluidic enzyme kinetics. *Science* 373(6553):eabf8761. https://doi.org/10.1126/science.abf8761
22. Sone N, Konishi S, Igura K et al (2021) Multicellular modeling of ciliopathy by combining iPS cells and microfluidic airway-on-a-chip technology. *Sci Transl Med* 13(601):eabb1298. https://doi.org/10.1126/scitranslmed.abb1298
23. Wang BF, Li YW, Zhou MF et al (2023) Smartphone-based platforms implementing microfluidic detection with image-based artificial intelligence. *Nat Commun* 14(1):1341. https://doi.org/10.1038/s41467-023-36017-x
24. Wang YH, Zheng GX, Jiang N et al (2023) Nature-inspired micropatterns. *Nat Rev Method Prim* 3:68. https://doi.org/10.1038/s43586-023-00251-w
25. Cho S, Shaban SM, Song RH et al (2024) A skin-interfaced microfluidic platform supports dynamic sweat biochemical analysis during human exercise. *Sci Transl Med* 16(763):eado5366. https://doi.org/10.1126/scitranslmed.ado5366
26. Yang N, Song W, Xiao Y et al (2024) Minimum minutes machine-learning microfluidic microbe monitoring method (M7). *ACS Nano* 18(6):4862–4870. https://doi.org/10.1021/acsnano.3c09733
27. Jiang LX, Li XT, Polack M et al (2026) High-spatial-resolution mass spectrometry imaging of biological tissues using a microfluidic probe. *Nat Protoc* 21(1):18–36. https://doi.org/10.1038/s41596-025-01188-y
28. Qin YZ, Koehler SA, Ling YY et al (2025) Fast, cost-effective and flexible DNA sequencing by roll-to-roll fluidics. *Nat Methods* 22(8):1662–1668. https://doi.org/10.1038/s41592-025-02730-2
29. Stringer M, Zeng ZM, Zhang XY et al (2023) Methodologies, technologies, and strategies for acoustic streaming-based acoustofluidics. *Appl Phys Rev* 10:011315. https://doi.org/10.1063/5.0134646
30. Rezk AR, Ahmed H, Ramesan S et al (2021) High frequency sonoprocessing: a new field of cavitation-free acoustic materials synthesis, processing, and manipulation. *Adv Sci* 8(1):2001983. https://doi.org/10.1002/advs.202001983
31. Cha B, Lee SH, Iqrar SA et al (2023) Rapid acoustofluidic mixing by ultrasonic surface acoustic wave-induced acoustic streaming flow. *Ultrason Sonochem* 99:106575. https://doi.org/10.1016/j.ultsonch.2023.106575
32. Biroun MH, Rahmati M, Jangi M et al (2021) Numerical and experimental investigations of interdigital transducer configurations for efficient droplet streaming and jetting induced by surface acoustic waves. *Int J Multiph Flow* 136:103545. https://doi.org/10.1016/j.ijmultiphaseflow.2020.103545
33. Maramizonouz S, Tao X, Rahmati M et al (2021) Flexible and bendable acoustofluidics for particle and cell patterning. *Int J Mech Sci* 202–203:106536. https://doi.org/10.1016/j.ijmecsci.2021.106536
34. Collins DJ, Ma ZC, Han J et al (2017) Continuous micro-vortex-based nanoparticle manipulation via focused surface acoustic waves. *Lab Chip* 17(1):91–103. https://doi.org/10.1039/c6lc01142j
35. Collins DJ, Khoo BL, Ma ZC et al (2017) Selective particle and cell capture in a continuous flow using micro-vortex acoustic streaming. *Lab Chip* 17(10):1769–1777. https://doi.org/10.1039/c7lc00215g
36. Reboud J, Bourquin Y, Wilson R et al (2012) Shaping acoustic fields as a toolset for microfluidic manipulations in diagnostic technologies. *Proc Natl Acad Sci USA* 109(38):15162–15167. https://doi.org/10.1073/pnas.1206055109
37. Wang SC, Lv XQ, Su Y et al (2019) Piezoelectric microchip for cell lysis through cell–microparticle collision within a microdroplet driven by surface acoustic wave oscillation. *Small* 15(9):1804593. https://doi.org/10.1002/smll.201804593
38. Wang WB, Chen YS, Farooq U et al (2017) Ultrafast chemical-free cell lysis by high speed stream collision induced by surface acoustic waves. *Appl Phys Lett* 110(14):143504. https://doi.org/10.1063/1.4979788
39. Nyborg WL (1965) Acoustic streaming. In: Mason WP (Ed.), Physical Acoustics. Academic Press, New York, USA, p.265–331
40. Zheng TF, Xu CP, Yang QY (2023) The effect of high-frequency acoustic wave vibration pattern on HKUST's multi-level pore structure. *Ultrason Sonochem* 95:106368.

https://doi.org/10.1016/j.ultsonch.2023.106368
41. Han JL, Hu H, Huang QY et al (2021) Particle separation by standing surface acoustic waves inside a sessile droplet. *Sens Actuat A Phys* 326:112731. https://doi.org/10.1016/j.sna.2021.112731
42. Wei W, Wang YP, Wang ZX et al (2023) Microscale acoustic streaming for biomedical and bioanalytical applications. *TrAC Trends Anal Chem* 160:116958. https://doi.org/10.1016/j.trac.2023.116958
43. Shen L, Tian ZH, Yang KC et al (2024) Acousto-dielectric tweezers enable independent manipulation of multiple particles. *Sci Adv* 10(32):eado8992. https://doi.org/10.1126/sciadv.ado8992
44. Gu YY, Chen CY, Mao ZM et al (2021) Acoustofluidic centrifuge for nanoparticle enrichment and separation. *Sci Adv* 7(1): eabc0467. https://doi.org/10.1126/sciadv.abc0467
45. Richard C, Fakhfouri A, Colditz M et al (2019) Blood platelet enrichment in mass-producible surface acoustic wave (SAW) driven microfluidic chips. *Lab Chip* 19(24):4043–4051. https://doi.org/10.1039/c9lc00804g
46. Mao ZM, Xie YL, Guo F et al (2016) Experimental and numerical studies on standing surface acoustic wave microfluidics. *Lab Chip* 16(3):515–524. https://doi.org/10.1039/c5lc00707k
47. Packard MM, Wheeler EK, Alocilja EC et al (2013) Performance evaluation of fast microfluidic thermal lysis of bacteria for diagnostic sample preparation. *Diagnostics* 3(1):105–116. https://doi.org/10.3390/diagnostics3010105